Combining orbit jump and potential wells optimizations for nonlinear vibration energy harvesters

C Saint-Martin, A Morel, L Charleux, E Roux, D Gibus, A Benhemou, A Badel

Combining Orbit Jump and Potential Wells Optimizations for Nonlinear Vibration Energy Harvesters

C. Saint-Martin,[1] A. Morel,[1] L. Charleux,[1] E. Roux,[1] D. Gibus,[1] A. Benhemou,[1] and A. Badel[1]
Savoie Mont Blanc University, SYMME, F-74000, Annecy, France

(*Electronic mail: camille.saint-martin@univ-smb.fr)

(Dated: 16 October 2023)

Nonlinear Vibration Energy Harvesters (VEHs) are widely used for scavenging vibrational energy due to their broadband behaviors. However, they exhibit multiple orbits of different powers for a given excitation, including low-power orbits that might limit their performance. To address this issue and enhance nonlinear VEHs performance, various studies have defined orbit jump strategies to transition from low-power to high-power orbits. Another way to maximize the power of nonlinear VEHs is to optimize their geometry by finely engineering their Potential Wells (PWs). In this letter, we propose an orbit jump strategy for bistable VEHs that combines the two latter approaches, i.e., that simultaneously optimizes their PWs while jumping from low-power to high-power orbits. This orbit jump strategy is optimized using a numerical criterion that takes into account the robustness of the jumps and the invested energy. The proposed orbit jump strategy has been experimentally validated for vibration frequencies between 30 and 60 Hz. It is shown that the proposed approach can increase the power by an average of 121 times over the considered frequency range. Compared to traditional orbit jump strategies, the proposed approach, which combines orbit jumping and PWs optimizations, increases by up to 3 times the harvested power.

Harvesting energy from ambient vibrations, a ubiquitous energy source, is a promising solution for powering wireless sensors and low-power electronic devices [1]. VEHs with nonlinearities[2], have gained significant attention due to their ability to operate over a wider frequency range compared to their linear counterparts [3,4]. In particular, nonlinear vibration energy harvesting presents two major challenges:

(i) Optimal PWs. The geometry of an energy harvester determines the shape of its PWs, which can result in poor energy harvesting performance. Indeed, for a given excitation, there is an optimal shape of the PWs that maximizes energy harvesting and improves the overall performance of the nonlinear VEH [5].

(ii) High-power orbit operation. The dynamics of nonlinear VEHs can exhibit both low-power and high-power orbits. Specific excitation conditions may lead to VEHs operating in low-power orbits, resulting in mediocre energy harvesting performance.

To address challenge (i), researchers have investigated the optimal potential shape of nonlinear VEHs, for a given excitation. This can be done by optimizing the design parameters of VEHs (e.g., the prototype geometry and materials). As a matter of example, Chen *et al.*[6] introduced a complex nonlinear VEH made with a linear and a nonlinear oscillators, coupled by a linear spring. They finely tuned the spring stiffness to optimize the PWs, resulting in a 70% increase in the effective bandwidth frequency compared to a traditional bistable VEH. Another approach, introduced by Hosseinlo *et al.*[7] consists in an adaptive bistable potential VEH that lowers its inter-well potential barrier when the mass is confined to one of the wells. The numerical results showed that the proposed technique led to a significant increase in harvested energy compared to a traditional bistable VEH. However, this active control requires a certain amount of power, and has yet to be validated experimentally. Liu *et al.*[8] designed a seesaw-inspired bistable VEH tailored to the real-world vibration conditions of train bogies. The PWs of the prototype are engineered and optimized by adjusting the spring lengths and magnet positions. While all these solutions are interesting to increase the harvested power of bistable VEHs, optimal PWs do not ensure high-power orbit operation, which is necessary to fully exploit the performance of nonlinear VEHs, especially under harmonic or quasi-harmonic excitation.

To address challenge (ii), researchers have explored orbit jump strategies that enable VEHs to transition from low-power to high-power orbits. On the one hand, researchers have used orbit jump strategies that introduce an external perturbation into the system[9,10]. On the other hand, researchers have used orbit jump strategies that temporarily modulate the parameters of the VEHs[11,12] (e.g., the buckling level or the stiffness). Similar to adaptive PWs methods, these orbit jump strategies require a certain amount of energy cost and time to achieve a positive energy balance. This has led to the optimization of existing orbit jump strategies to reduce their energy costs [13]. Although traditional orbit jump strategies enable high-power orbit operation, they do not optimize the intrinsic performance of nonlinear VEHs by finely engineering their PWs.

In this letter, we propose an approach that addresses the two challenges (i) and (ii) of nonlinear VEHs by simultaneously combining orbit jump strategy and PWs optimizations. Orbit jumps are implemented by tuning the buckling level of the nonlinear VEH to achieve optimal PWs.

Figure 1 compares the proposed approach with traditional orbit jump strategies from the literature. Traditional orbit jump strategies, shown on the left, allow jumping without optimizing PWs; however, the orbit jump strategy proposed in this letter, shown on the right, differs by using PWs optimization for the jump. Therefore, the effects of the orbit jump strategy are twofold: achieving optimal PWs (depicted in red) and jumping from low-power to high orbits, as shown in Fig.1.

The nonlinear VEH considered in this study, shown in

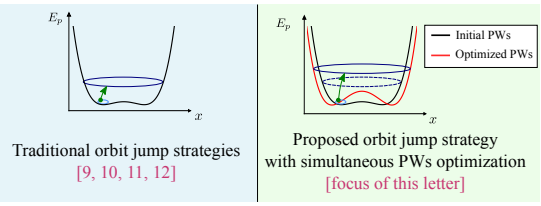

FIG. 1. Comparison of the proposed approach with traditional orbit jump strategies. The dashed high orbit corresponds to the high orbit obtained with a traditional orbit jump strategy, i.e., without PWs optimization.

Fig.6, was designed by Benhemou *et al.*[14]. It consists of a bistable mechanical oscillator with mass M, composed of buckled steel beams of length L. The oscillator has two stable equilibrium positions located at $x = \pm x_w$. The considered VEH includes two Amplified Piezoelectric Actuators (APAs). The smaller APA, called the *Energy harvesting APA*, is used to extract energy from the mechanical oscillator. It exhibits a force factor α and a clamped capacitance C_p. The second and stiffer APA, called *Tuning APA*, is used temporarily to implement the proposed orbit jump strategy by adjusting the buckling level of the prototype, implying a change in the equilibrium position x_w. The electrodes of the energy harvesting APA are connected to a resistor denoted by R. In this study, we assume a harmonic excitation, with a constant acceleration amplitude A and a driving angular frequency ω_d. Under this assumption, the focus is on harmonic and quasi-harmonic ambient excitations, which can be found in many applications. This is the case, for example, for industrial machine vibrations that have a single dominant peak in their vibration spectrum[15].

The dynamics of the piezoelectric bistable VEH is described by the following system[11] of nonlinear Ordinary Differential Equations (ODEs):

$$\begin{cases} \ddot{x} + \dfrac{\omega_0^2}{2}\left(\dfrac{x^2}{x_w^2} - 1\right)x + \dfrac{\omega_0}{Q}\dot{x} + 2\dfrac{\alpha}{ML}xv = A\sin(\omega_d t) & \text{(1a)} \\ \dfrac{2\alpha}{L}x\dot{x} = C_p\dot{v} + \dfrac{1}{R}v & \text{(1b)} \end{cases}$$

The variables x, $\dot{x}$ and $\ddot{x}$ represent the displacement, velocity and acceleration of the mass, respectively. The voltage across the energy harvesting APA is denoted by v. ω_0 and Q represent the natural angular frequency and the mechanical quality factor of the linearized model of the VEH, respectively, as defined by Liu *et al.*[16]. Table I provides the parameter values of the bistable VEH considered in this study, which have been determined with low acceleration characterizations. Equation (1a) expresses the mechanical dynamics with an electromechanical coupling term $\left(2\dfrac{\alpha}{ML}xv\right)$ that illustrates the impact of the voltage on the VEH mass displacement. Equation (1b) models the electrical dynamics with an electromechanical coupling term $\left(\dfrac{2\alpha}{L}x\dot{x}\right)$ that represents the current generated by the piezoelectric effect. It is worth noting that there is no term associated with the tuning APA due to its higher stiffness compared to the energy harvesting APA. Therefore, its influence on VEH dynamics is assumed to be negligible. The elastic potential energy of the considered bistable VEH is obtained by integrating the nonlinear elastic force $-\dfrac{M\omega_0^2}{2}\left(\dfrac{x^2}{x_w^2} - 1\right)x$ in Eq.2.

Parameters	Symbols	Values	Units
Stable equilibrium positions	$\pm x_w$	± 0.62	mm
Proof mass	M	6	g
Horizontal distance from the mass to the frame	L	35	mm
Natural angular frequency	ω_0	295	rad/s
Mechanical quality factor	Q	160	
Piezoelectric force factor	α	0.14	N/V
Piezoelectric clamped capacitance	C_p	1	µF

TABLE I. Identified parameter values of the nonlinear VEH prototype [14], shown in Fig.6.

$$\begin{aligned} E_p(t) &= \frac{M\omega_0^2}{2}\int\left(\frac{x^2}{x_w^2} - 1\right)x\,dx \\ &= \frac{M\omega_0^2}{8x_w^2}\left(x(t) + x_w\right)^2\left(x(t) - x_w\right)^2 \end{aligned} \quad (2)$$

As highlighted in several studies, bistable VEHs exhibit multiple possible orbits for a given driving frequency [17,18]. For example, at a frequency of 55 Hz, the numerically harvested power in high orbit is 244 times larger than the power in low orbit. If the VEH oscillates in low-power orbits, applying an orbit jump strategy or adjusting the PWs of the VEH can significantly improve its performance.

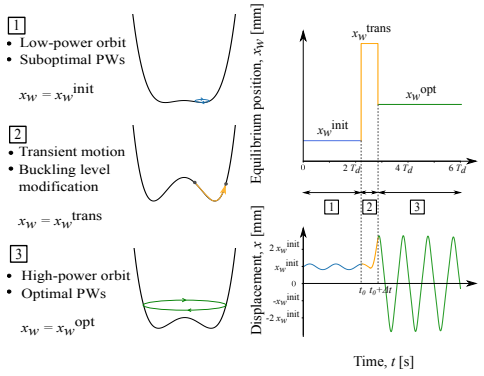

FIG. 2. Description of the three different steps of the orbit jump strategy. $x_w^{\text{init}} = 0.62$ mm represents the initial (suboptimal) value of the buckling level.

The orbit jump strategy considered in this study is an extension of the orbit jump strategy developed by Huguet *et al.*[11] and subsequently optimized in [13]. The corresponding strategy is based on modifying the buckling level to jump from low-power to high orbits, as well as optimizing the PWs. The strategy depends on four parameters: t_0, the starting time of the orbit jump, Δt, the duration of the jump, x_w^{trans}, the buckling level during the jump and x_w^{opt}, the final buckling level

after the jump. The three steps of the orbit jump, as illustrated in Fig.2, are as follows:

Step 1: Before the orbit jump (before t_0), the VEH oscillates in low-power orbit around x_w^{init}, which is one of the two stable positions in the PWs whose shape is fixed by the oscillator geometry. As seen in the upper left of the Fig.2, the VEH is stuck in a low orbit.

Step 2: During the orbit jump (between t_0 and $t_0+\Delta t$), the buckling level of the VEH is increased to x_w^{trans} due to the change in the voltage of the tuning APA. As a result, potential energy is transferred to the mass when $t=t_0$ and $t=t_0+\Delta t$. As shown in the center left of the Fig.2, the VEH oscillates temporarily with a deeper PWs.

Step 3: After the orbit jump (from $t_0+\Delta t$), the buckling level of the VEH is held at its final value x_w^{opt}. The final PWs, in comparison to the initial PWs, result in more powerful high orbits, thus enhancing the VEH performances. As seen in the bottom left of the Fig.2, the final PWs are deeper than the original ones and require then more energy to overcome the potential barrier.

As described in Eq.2, the potential barrier increases with the buckling level of the bistable VEH, as shown in Fig.2 for $x_w = x_w^{\text{trans}}$. The energy invested during the jump is equal to the potential energy difference between t_0 and $t_0+\Delta t$, and can be computed from (2):

$$\begin{aligned} E_{\text{inv}}(t_0,\Delta t,x_w^{\text{trans}},x_w^{\text{opt}}) &= E_p(t_0^+) - E_p(t_0^-) \\ &\quad + E_p[(t_0+\Delta t)^+] - E_p[(t_0+\Delta t)^-] \\ &= \Delta E_0 + \Delta E_1 \end{aligned} \tag{3}$$

Where ΔE_0 (resp. ΔE_1) represents the potential energy difference at time t_0, where t_0^- (resp. $(t_0+\Delta t)^-$) and t_0^+ (resp. $(t_0+\Delta t)^+$) denote the times immediately before and after t_0 (resp. $t_0+\Delta t$), respectively.

We conducted a numerical investigation to determine the optimal parameter values $(t_0,\Delta t,x_w^{\text{trans}},x_w^{\text{opt}})$ of the orbit jump strategy that maximizes both its performance and its robustness for driving frequencies between 30 and 60 Hz. The performance of the orbit jump can be evaluated by calculating the harvested energy over 100 cycles, from which we subtract the invested energy (3) as given in Eq.4.

$$E_{\text{tot}}(t_0,\Delta t,x_w^{\text{trans}},x_w^{\text{opt}}) = \overbrace{\int_0^{100\,T_d} \frac{v(t)^2}{R} dt}^{\textbf{Harvested energy}} - \underbrace{E_{\text{inv}}(t_0,\Delta t,x_w^{\text{trans}},x_w^{\text{opt}})}_{\textbf{Invested energy}} \tag{4}$$

On the other hand, it is necessary to determine parameters that not only maximize E_{tot}, but are also sufficiently robust to reproduce the orbit jump experimentally, even with experimental uncertainties on the jump parameters. In this work, this robustness is assessed by averaging the total energy harvested, E_{tot}, (4) in a neighborhood of a given combination of jump parameters $(t_0,\Delta t,x_w^{\text{trans}},x_w^{\text{opt}})$ (with a variation of $\pm 10\%$ on each parameter), whose expression is given Eq.5.

$$\overline{E_{\text{tot}}}(t_0,\Delta t,x_w^{\text{trans}},x_w^{\text{opt}}) = \sum_{i=0}^{N-1} E_{\text{tot}}(t_0^i,\Delta t^i,x_w^{\text{trans},i},x_w^{\text{opt},i}) \Big/ N \tag{5}$$

Where $N>1$, integer, the number of jump parameter combinations tested in the neighborhood of a given combination $(t_0,\Delta t,x_w^{\text{trans}},x_w^{\text{opt}})$. Eq.5 is the objective function to be maximized in order to ensure performant and robust jumps. The optimization method consists in simulating a large number of jump parameter combinations for driving frequencies between 30 and 60 Hz. An example of such a neighborhood uniformly distributed around a given parameter combination (represented by a red point) is shown in green in Fig.3.

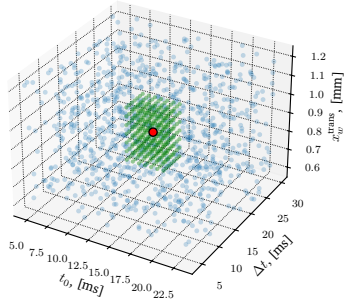

FIG. 3. Vizualization of a neighborhood (green points) around a given parameter combination (red point) among a set of jump parameter combinations (blue points) in the 3D plane $(t_0,\Delta t,x_w^{\text{trans}})$.

We developed a dedicated Python CUDA code that takes advantage of parallel computing on GPUs for optimizing $\overline{E_{\text{tot}}}$. Using the Dormand-Prince method [19], we solved the nonlinear ODEs Eq.1 starting from the low-power orbit, for a large number of jump parameter combinations (4 million per frequency). We then selected the best combination of jump parameter for all driving frequencies. Figure 4 shows the evolution of the optimal jump parameter combinations $(t_0/T_d,\Delta t/T_d,x_w^{\text{trans}},x_w^{\text{opt}})$ as a function of the driving frequency. It is worth mentioning that the staircase shape of the optimal curves in Fig.4 stems from an exhaustive optimization analysis within a 4 million point grid, with each step indicating a shift to a new optimal value in this grid. The sudden change in the starting time evolution at 35 Hz (Fig.4(a)) can be attributed to the softening nonlinearity of the low-power intra-well orbits[13]. In Fig.4(d), the optimal final buckling level decreases from 39 Hz, corresponding to a lower optimal potential barrier that ensures the transition to the final high-power orbit. As a result, we select the final orbit with the highest amplitude and the least sensitivity to parameter variations and external disturbances for each driving frequency. Note that the duration and the buckling level of the transient motion increase with the driving frequency (Fig.4(b,c)). This can be justified by the fact that the gap between low and high orbits increases with the driving frequency.

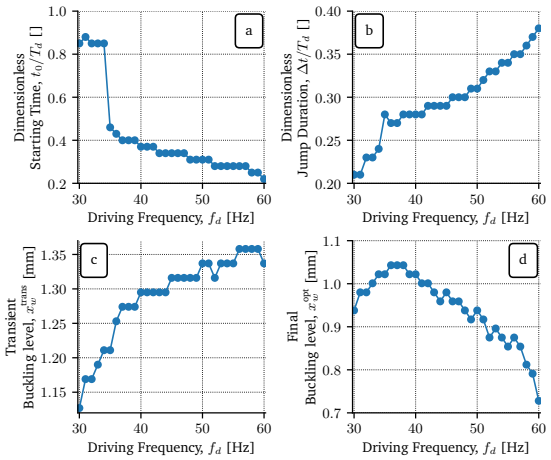

FIG. 4. Optimal jump parameter values: (a) dimensionless starting time t_0/T_d, (b) dimensionless jumping time $\Delta t/T_d$, (c) transient buckling level x_w^{trans} and (d) final buckling level x_w^{opt} as a function of the driving frequency.

Figure 5 compares the final orbits at 30 Hz for two orbit jump strategies: one strategy implements the optimization of the final PWs (shown in green), while the other maintains the final buckling level to be identical to the initial one (shown in magenta). As seen in Fig.5, the displacement amplitude x with the optimized final orbit is greater than the amplitude without optimization, resulting in a power output of 0.36 mW as opposed to a lower 0.13 mW without optimization. Indeed, since the power is directly proportional to the square of the displacement amplitude [20], optimizing the PWs at this frequency can notably enhance energy harvesting performance. Note that without any orbit jump, the power would be much lower, around 4 μW, which corresponds to the power of the initial low orbit.

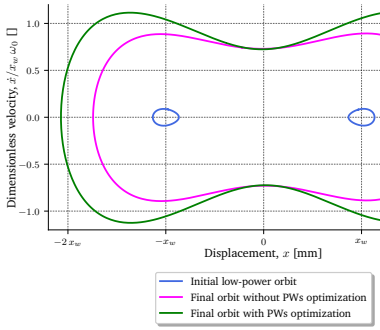

FIG. 5. Comparison of the final orbits with (in green) and without (in magenta) optimization of the final buckling level for $f_d = 30$ Hz and $A = 3$ m/s^2. Note that x_w notation on the axes corresponds to the initial buckling level of the bistable VEH, x_w^{init}.

Figure 6 shows the bistable prototype mounted on the electromagnetic shaker and the global experimental setup. The experimental setup consists of an accelerometer measuring the acceleration amplitude of the shaker, a laser differential vibrometer measuring both the displacement x and velocity $\dot{x}$

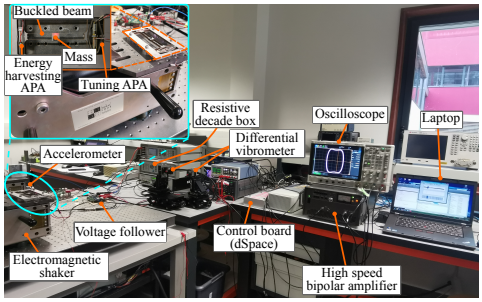

FIG. 6. Experimental setup and experimental bistable VEH prototype [14].

of the mass, a control board (dSpace) for real-time control of several variables (e.g., the acceleration amplitude of the sinusoidal excitation A or the voltage across the tuning APA v_w), a resistive decade box to adjust the load resistance value. Note that prior to any experimental testing, we identified the VEH prototype parameter values (Table I) in low-power orbit using weak sinusoidal oscillations and based our optimization on these identified VEH parameter values. The quality factor value was obtained in a frequency sweep to adjust its value in high orbits, which is lower than in low orbits. We launch several experimental tests of jump parameter combinations in the frequency range [30 Hz, 60 Hz] in order to validate both the efficiency and the robustness of the approach.

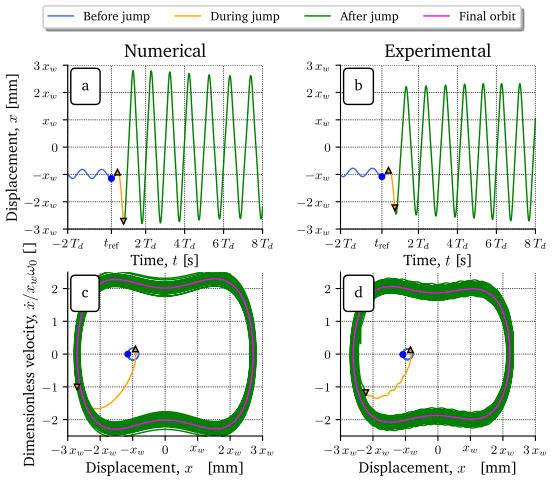

FIG. 7. Comparison between numerical (a,c) and experimental (b,d) trajectories for in the phase plane $(x, \dot{x}/x_w\,\omega_0)$ for 50 Hz before (in blue), during (in orange) and after (in green). Blue points correspond to the beginning of the orbit jump process (the corresponding time is denoted by t_{ref}), triangle up (resp. down) markers refer to the moment when the buckling level is increased in step 2 (resp. reaches its final value in step 3). The final orbits are drawn in magenta. Note that x_w means x_w^{init}. Numerical jump parameter values $(t_0/T_d, \Delta t/T_d, x_w^{\text{trans}}, x_w^{\text{opt}}) = (0.31, 0.31, 1.34, 0.96)$. Experimental jump parameter values $(t_0/T_d, \Delta t/T_d, x_w^{\text{trans}}, x_w^{\text{opt}}) = (0.31, 0.33, 1.34, 0.96)$.

Figure 7 compares experimental and numerical trajectories

in both time and phase planes at 50 Hz while implementing the orbit jump with optimization of the final PWs. As seen in Fig.7, the results are fairly close, although the experimental trajectory shows slight asymmetries. These may be due to the assembly and mechanical irregularities in the manufacturing process of the experimental VEH prototype. The perturbations in the experimental transient trajectory may be due to the rapid variation of the buckling level, leading to the excitation of higher modes of the bistable VEH, which are not taken into account in the model.

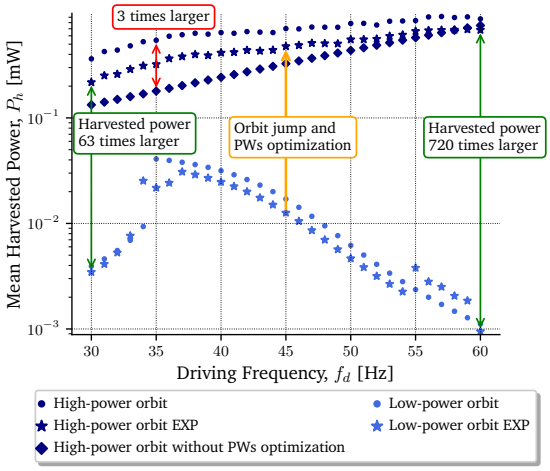

FIG. 8. Evolution of the mean harvested power as a function of the driving frequency for numerical (indicated by dots) and experimental (indicated by stars) data, respectively.

Figure 8 shows the mean harvested power for both experimental (indicated by stars) and numerical (indicated by dots or diamonds) results. The experimental powers were obtained from the orbit jump experiments. The numerical powers indicated by diamonds correspond to orbit jumps without PWs optimization. As seen in Fig.8, for frequencies equal to or greater than 55 Hz, there is a difference in the experimental power of the low-power orbit that could be due to a slight uncontrolled initial buckling variation of the VEH prototype during experimental testing.

Figure 8 shows the significant benefits of the orbit jump strategy, which increases the harvested power by up to 720 times between the low-power and high-power orbits at 60 Hz. Compared to traditional orbit jump strategies (dark blue diamonds), optimizing the PWs (dark blue stars and dots) results in, at most, a 3-fold increase in the numerical power of high-power orbits in the frequency range 30 Hz – 45 Hz. For example, at 40 Hz, the power of the high-power orbit is 0.64 mW with PWs optimization, compared to 0.24 mW without optimization. Note that without any orbit jump, the output power remains much lower, around 31 µW. The optimization of PWs beyond 45 Hz becomes less beneficial. This is due to the decrease in the value of the optimal buckling level with frequency (see Fig.4(d)), which gets closer to the initial buckling level. Differences between numerical and experimental results may be attributed to inaccuracies in the parameter identification or in the modeling of the orbit jump, which involves numerous parameters. Indeed, the orbit jump requires the adjustment of four jump parameters, resulting in a chain of uncertainties due to experimental parameter control. The power differences observed in the low-power orbit in 34 Hz – 36 Hz could result from discrepancies between the numerical and experimental models of the VEH prototype (e.g., asymmetries and/or inaccuracies in identified parameter values).

References	Excitation	Energy cost	Recovery time	Power increase	Simultaneous PWs optimization
Yan[21] *et al.* (2019)	Multiple freq. 48.6 – 49.5 Hz 3.82 m/s^2	1.43 mJ	23 s	×25	✗
Ushiki[22] *et al.* (2019)	Single freq. 70 Hz 1.962 m/s^2	35 mJ*	20 s	×30*	✗
Huang[23] *et al.* (2022)	Multiple freq. 35 – 40 Hz 5 m/s^2	4.67 mJ	120 s	×208	✗
Zhao[24] *et al.* (2023)	Multiple freq. 6.7 – 7.8 Hz 1 m/s^2	11.2 mJ	120 s	×9.1	✗
This letter (2023)	Multiple freq. 30 – 60 Hz 3 m/s^2	0.5 mJ$^\diamondsuit$	1 s$^\diamondsuit$	×121$^\diamondsuit$	✓

TABLE II. Comparison between the optimized orbit jump strategy developed in this letter and other traditional orbit jump strategies in the literature. * indicates that the values have been estimated based on the given papers. The values corresponding to this letter are marked with $^\diamondsuit$ to indicate that they are averaged over the frequency range [30 Hz, 60 Hz].

Table II compares the proposed orbit jump strategy with other orbit jump strategies from the literature according to the excitation configuration, the invested energy, the time required to recover the energy cost, the increase in power, and whether they optimized the PWs. The respective approaches of Yan[21] and Ushiki[22] achieved maximum enhancements after the jump, by factors of 25 and 30, respectively. Huang[23] proposed to combine two orbit jump strategies, which resulted in a significant recovery time, but increased the power by 208 times. Zhao[24] investigated a solution for simultaneous orbit jumping and energy extraction, which required a long time to recover the energy invested, while increasing the harvested power after the jump by a factor of 9.1. Importantly, only the orbit jump strategy in this letter changes the shape of the PWs at the end of the jump. This optimization improves the power of the high orbits and decreases the recovery time. For values corresponding to this letter, averages of the invested energy, recovery time, and power increase have been calculated to allow comparison with other orbit jump strategies in the literature. Notably, the proposed orbit jump strategy results in a short average recovery time of only 1 s and a mean power increase of 121 times over the 30 – 60 Hz frequency range. These results are enabled by the unique combination of a numerically optimized orbit jump and simultaneous PWs optimization, which further enhances the performance of nonlinear VEHs.

It is worth mentioning the practical challenges may arise while implementing the proposed orbit jump strategy. Indeed, implementing such orbit jump strategy in a self-powered manner will require designing a system for detecting the initial orbit of the system, sensing the driving frequency, and precisely timing the instants of jump. To detect the VEH

orbit, an electronic system measuring the voltage amplitude across the piezoelectric materials could be used. Indeed, from this information, it is possible to know whether the system is in high-power orbit (with large voltage amplitude), or low-power orbit (with low voltage amplitude). In order to properly implement the orbit jump, with optimal parameters, the results of a numerical optimization (such as the one performed in this letter) should be stored in an on-chip memory in order to provide the system with the optimal values of $(t_0, \Delta t, x_w^{\text{trans}}, x_w^{\text{opt}})$. Such practical implementation could be facilitated by ultra-low power sensing and self-powered power management integrated circuits[25–27] that consume less than 10 μW, a negligible consumption compared to the power generated in the high orbit (414 μW at 40 Hz).

In conclusion, this work has proposed an orbit jump strategy that allows not only to change the orbit, but also to shape the PWs at the end of the jump, which further enhances the harvested power. The PWs adaptation has proven particularly effective at low frequencies, between 30 and 45 Hz. The optimized orbit jump strategy was experimentally validated between 30 and 60 Hz, demonstrating its robustness. By optimizing the shape of the PWs, the harvested power has been increased up to three times compared to traditional orbit jump strategies. This work paves the way toward self-adaptive nonlinear VEHs which could optimize their PWs depending on the ambient vibration characteristics, while continuously operating in high-power orbits.

ACKNOWLEDGMENTS

This project has received funding from the European Union's Horizon 2020 research and innovation program under grant agreement No 862289.

[1] C. Wei and X. Jing, "A comprehensive review on vibration energy harvesting: Modelling and realization," Renewable Sustainable Energy Rev. **74**, 1–18 (2017).

[2] S. Fang, S. Zhou, D. Yurchenko, T. Yang, and W.-H. Liao, "Multistability phenomenon in signal processing, energy harvesting, composite structures, and metamaterials: A review," Mech. Syst. Signal Process. **166**, 108419 (2022).

[3] R. L. Harne and K. W. Wang, "A review of the recent research on vibration energy harvesting via bistable systems," Smart Mater. Struct. **22**, 023001 (2013).

[4] S. Zhou, M. Lallart, and A. Erturk, "Multistable vibration energy harvesters: Principle, progress, and perspectives," J. Sound Vib. **528**, 116886 (2022).

[5] J. Cao, S. Zhou, W.-J. Wang, W. Wei, and J. Lin, "Influence of Potential Well Depth on Nonlinear Tristable Energy Harvesting," Appl. Phys. Lett. **106**, 173903 (2015).

[6] K. Chen, X. Zhang, X. Xiang, H. Shen, Q. Yang, J. Wang, and G. Litak, "High performance piezoelectric energy harvester with dual-coupling beams and bistable configurations," Journal of Sound and Vibration **561**, 117822 (2023).

[7] A. H. Hosseinloo and K. Turitsyn, "Non-resonant energy harvesting via an adaptive bistable potential," Smart Mater. Struct. (2015), 10.1088/0964-1726/25/1/015010.

[8] M. Liu, Y. Zhang, H. Fu, Y. Qin, A. Ding, and E. M. Yeatman, "A seesaw-inspired bistable energy harvester with adjustable potential wells for self-powered internet of train monitoring," Appl. Energy (2023), 10.1016/j.apenergy.2023.120908.

[9] D. Mallick, A. Amann, and S. Roy, "Surfing the High Energy Output Branch of Nonlinear Energy Harvesters," Phys. Rev. Lett. **117**, 197701 (2016).

[10] S. Zhou, J. Cao, D. J. Inman, S. Liu, W. Wang, and J. Lin, "Impact-induced high-energy orbits of nonlinear energy harvesters," Appl. Phys. Lett. **106**, 093901 (2015).

[11] T. Huguet, M. Lallart, and A. Badel, "Orbit jump in bistable energy harvesters through buckling level modification," Mech. Syst. Signal Process. **128**, 202–215 (2019).

[12] J. Wang and W.-H. Liao, "Attaining the high-energy orbit of nonlinear energy harvesters by load perturbation," Energy Convers. Manag. **192**, 30–36 (2019).

[13] C. Saint-Martin, A. Morel, L. Charleux, E. Roux, D. Gibus, A. Benhemou, and A. Badel, "Optimized and Robust Orbit Jump for Nonlinear Vibration Energy Harvesting," (2023), in process of submission.

[14] A. Benhemou, T. Huguet, D. Gibus, C. Saint-Martin, Q. Demouron, A. Morel, E. Roux, L. Charleux, and A. Badel, "Predictive modelling approach for a piezoelectric bistable energy harvester architecture," in *2022 21st International Conference on Micro and Nanotechnology for Power Generation and Energy Conversion Applications PowerMEMS* (2022) pp. 106–109.

[15] R. Rantz and S. Roundy, "Characterization of real-world vibration sources with a view toward optimal energy harvesting architectures," in *SPIE Smart Structures and Materials + Nondestructive Evaluation and Health Monitoring*, edited by S. F. Griffin (Las Vegas, Nevada, United States, 2016) p. 98010P.

[16] W. Q. Liu, A. Badel, F. Formosa, Y. P. Wu, and A. Agbossou, "Novel piezoelectric bistable oscillator architecture for wideband vibration energy harvesting," Smart Mater. Struct. **22**, 035013 (2013).

[17] T. Huguet, A. Badel, and M. Lallart, "Exploiting bistable oscillator subharmonics for magnified broadband vibration energy harvesting," Appl. Phys. Lett. **111**, 173905 (2017).

[18] C. Saint-Martin, A. Morel, L. Charleux, E. Roux, A. Benhemou, and A. Badel, "Power expectation as a unified metric for the evaluation of vibration energy harvesters," Mech. Syst. Signal Process. **181**, 109482 (2022).

[19] J. Dormand and P. Prince, "A family of embedded Runge-Kutta formulae," J. Comput. Appl. Math. **6**, 19–26 (1980).

[20] A. Morel, L. Charleux, Q. Demouron, A. Benhemou, D. Gibus, C. Saint-Martin, A. Carré, E. Roux, T. Huguet, and A. Badel, "Simple analytical models and analysis of bistable vibration energy harvesters," Smart Mater. Struct. **31**, 105016 (2022).

[21] L. Yan, A. Badel, M. Lallart, and A. Karami, "Low-cost orbit jump in nonlinear energy harvesters through energy-efficient stiffness modulation," Sens. Actuator A Phys. **285**, 676–684 (2019).

[22] S. Ushiki and A. Masuda, "Toward self-powered nonlinear wideband vibration energy harvesting with high-energy response stabilization," J Phys Conf Ser **1407**, 012011 (2019).

[23] Y. Huang, Z. Zhao, and W. Liu, "Systematic adjustment strategy of a nonlinear beam generator for high-energy orbit," Mech. Syst. Signal Process. **166**, 108444 (2022).

[24] B. Zhao, J. Wang, G. Hu, A. Colombi, W. Liao, and J. Liang, "Time-sharing orbit jump and energy harvesting in nonlinear piezoelectric energy harvesters using a synchronous switch circuit," Mech. Syst. Signal Process. (2023), 10.1016/j.ymssp.2023.110601.

[25] A. Morel, A. Quelen, C. A. Berlitz, D. Gibus, P. Gasnier, A. Badel, and G. Pillonnet, "32.2 Self-Tunable Phase-Shifted SECE Piezoelectric Energy-Harvesting IC with a 30nW MPPT Achieving 446% Energy-Bandwidth Improvement and 94% Efficiency," in *2020 IEEE International Solid- State Circuits Conference - (ISSCC)* (IEEE, San Francisco, CA, USA, 2020) pp. 488–490.

[26] Xinling Y., Sundeep J., Zhong T., K. M., and S. D., "30.3 A Bias-Flip Rectifier with a Duty-Cycle-Based MPPT Algorithm for Piezoelectric Energy Harvesting with 98% Peak MPPT Efficiency and 738% Energy-Extraction Enhancement," IEEE International Solid-State Circuits Conference (2023), 10.1109/isscc42615.2023.10067284.

[27] Chao X., Guangshu Z., Yuan M., M. L., and Milin Z., "Fully Integrated Frequency-Tuning Switched-Capacitor Rectifier for Piezoelectric Energy Harvesting," IEEE Journal of Solid-State Circuits (2023), 10.1109/jssc.2023.3261301.